applied optics

Quantifying bio-filament morphology below the diffraction limit of an optical microscope using out-of-focus images

Madeleine Anthonisen,[1,*] Yuning Zhang,[1,2] M. Hussain Sangji,[3] and Peter Grütter[1]

[1]McGill University, Physics Department, 3600 rue Université, Montréal, Québec H3A2T8, Canada
[2]BGI-Research, 146 BeiShan Rd., Shenzhen 518083, China
[3]Biomedical Engineering Department, Northwestern University, 2145 Sheridan Rd., Evanston, Illinois 60208, USA
*Corresponding author: madeleine.anthonisen@mail.mcgill.ca

Received 14 January 2020; revised 13 February 2020; accepted 24 February 2020; posted 26 February 2020 (Doc. ID 388265); published 19 March 2020

A method to measure the dimensions of objects below the optical diffraction limit using diffraction analysis of out-of-focus bright-field images is presented. The method relies on the comparison of the diffraction patterns of an object of unknown size to those of calibration objects of known size. Correlative scanning electron microscope measurements are used to demonstrate the applicability of this method to measure 100 nm microbeads as well as objects with a geometry different from the calibration objects. This technique is important in the context of tethered particle experiments, in which bio-filaments are bound between a substrate and a microbead. This procedure is applied to obtain the diameters of axonal extensions or neurites that are mechanically created in samples of rat hippocampal neurons. The dependence of neurite geometry on mechanical pull speed is investigated, and the diameter is found to be rate independent.

https://doi.org/10.1364/AO.388265

1. INTRODUCTION

There is a class of biological force measurement techniques that relies on the manipulation of a microbead to induce the formation of a tether from a cell. Examples include optical tweezers experiments to extract and measure tension in tethers containing lipids and/or cytoskeleton elements [1–5] as well as experiments where a bead is aspirated and maneuvered with a micropipette to create a long, tubular structure [6,7]. In all of these examples, the tubes created have radii below the lateral diffraction limit of the optical microscope, ∼250 nm [8]. Electron microscopy (EM) is a powerful tool to get higher-resolution measurements and was exploited to measure fiber radii in Refs. [4,5]. However, the sample preparation process for EM involves fixation, which eliminates observation of cell dynamics and can cause morphological changes [9,10].

Bright-field microscopy has the advantage of being able to observe unstained samples continuously for long periods (several days). However, a feature of conventional bright-field microscopy is limited contrast when observing near-transparent samples such as cells [11]. These can be effectively invisible in focus but become visible when the microscope is slightly defocused [see Fig. 1(a)] [11–13]. In the defocused state, small objects (∼10 μm) create diffraction fringes in an image; even with a broad-band light source, the objects are within a coherence area [13]. In this work, a method for measuring the dimension of individual structures below the diffraction limit that requires only an optical microscope/camera and calibration objects of known dimensions is presented. We image the diffraction patterns created by an object of unknown size and a calibration object of known size in the same out-of-focus image. By comparing these patterns to those in a so-called "calibration series" of out-of-focus images of objects of known dimension, the diameter of the unknown object can be determined to ∼15% uncertainty, for diameters as small as ∼100 nm. This method is ideally suited for the class of experiments described above that features an object of known size (the microbead) together with a tether of unknown size. This method is validated by comparing diameters measured in this way to those obtained from scanning electron microscope (SEM) images of the same objects.

The scientific value of this method is demonstrated by applying it to determine the diameter of neurites created by mechanical pulling in samples of rat hippocampal neurons (see Fig. 1). Previous work [14] has shown that when a polystyrene bead coated with the polymer poly-D-lysine (PDL) contacts axons or dendrites, presynaptic structures form, which adhere to the bead. If the bead is pulled (in our case with a microneedle), the growth of an auxiliary structure, the neurite, is induced [7,15,16]. These neurites are cylindrical structures with

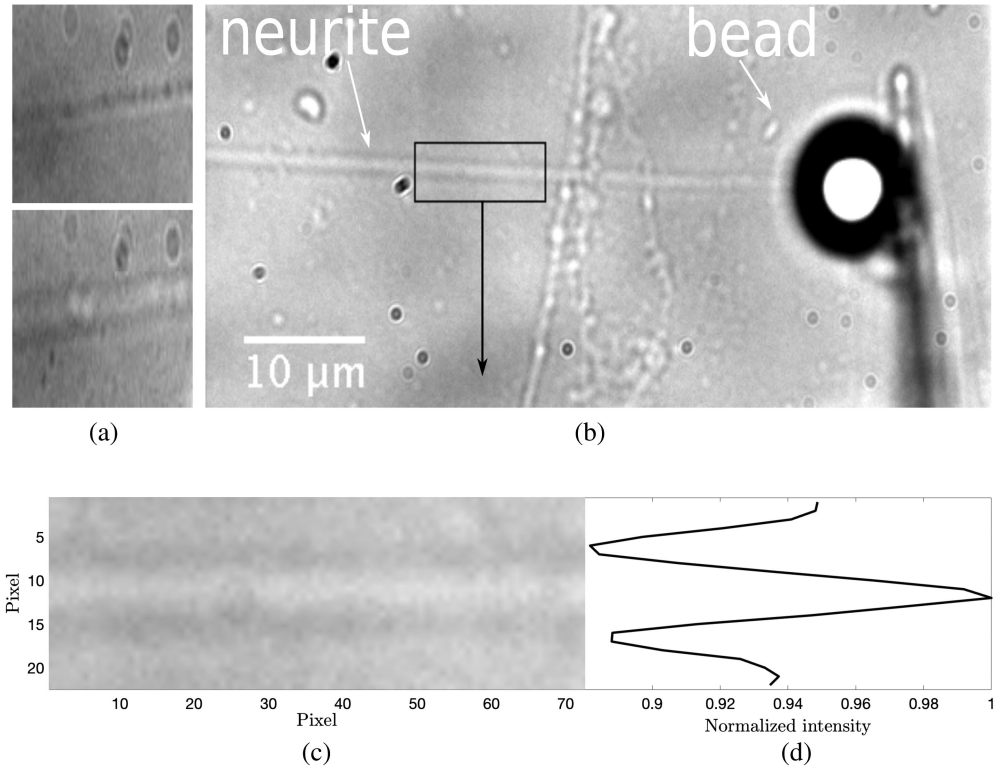

Fig. 1. (a) Nearly focused image of a (top) neurite compared to (bottom) a more defocused image. (b) Optical image of a neurite that is mechanically induced with a PDL-coated bead. (c) Isolated image of the neurite that has been rotated so its longitudinal axis is horizontal. (d) Both the neurite and the bead create diffraction patterns that can be used to extract the neurite diameter.

diameters near the diffraction limit [7]. In the following, this technique is used to investigate whether the diameter of neurites is affected by how fast they are pulled. This result has important implications for questions of what limits neuronal growth and regeneration [17–19] as well as for experiments that seek to re-wire neuronal networks with existing neurons [15,16,20].

In Section 1.1, the theoretical underpinnings of the experimental results are briefly outlined. In Section 2, a description of the method and correlative measurements are presented. Then in Section 3, the method is applied to biological filaments. Conclusions are presented in Section 4.

A. Diffraction Theory Concepts

The physical limitations of the optical microscope are due to a phenomenon called diffraction [21,22]. The intensity distribution of an optical wave that travels a given distance in free space after either being transmitted through an aperture in an opaque screen or encountering an object is known as the diffraction pattern [21–23]. Light will bend slightly at the edges of an object or an aperture. When light emitted from a point in the specimen is diffracted by the objective aperture of the microscope, it generates a blur in the image plane that is broader than the source. The light distribution from a point source is the point spread function (PSF). Mathematically, if the source is on axis, the PSF of an idealized system can be described by an Airy function [21,22]. In a single plane, this pattern consists of a central disk surrounded by rings. The diameter of this disk, known as the Airy disk, which depends on the wavelength of the illuminating light λ and the numerical aperture (NA) of the objective, is $\rho_d = 1.22\lambda/\mathrm{NA}$, which is ~ 250 nm for most microscopes. The Airy disk determines how close two equal point sources can be in the field of view and still be resolved as separate objects. In bright-field microscopy, the sample is illuminated with white light from above (or below) and observed from below (or above).

In classic fluorescence microscopy, the image intensity, $I_{\mathrm{em}}(\mathbf{x})$ at a postion $\mathbf{x}$, can be expressed as the convolution of the product of the illumination source, $I_{\mathrm{ex}}(\mathbf{x})$, a constant, and the sample distribution $s(\mathbf{x})$ with the PSF [11]:

$$I_{\mathrm{em}}(\mathbf{x}) = (I_{\mathrm{ex}}(\mathbf{x})s(\mathbf{x})) \circledast \mathrm{PSF}(\mathbf{x}). \tag{1}$$

If the PSF of the microscope is known, the intensity distribution of the object can be obtained precisely through deconvolution.

For bright-field microscopy, the deconvolution process is more complicated because the PSF is not unique. Reference [24] showed that the image formation process is described by two different PSFs: one that captures the phase structure of the object $\mathrm{PSF_P}$ and one that captures the absorption structure $\mathrm{PSF_A}$. The 3D intensity distribution of the object I_{em} is given in terms of the real part P and the imaginary part A of the scattering potential [11,24]:

$$I_{\mathrm{em}} = P \circledast \mathrm{PSF_P} + A \circledast \mathrm{PSF_A} + B, \tag{2}$$

where B is background light that does not interact with the sample. In most biological applications of bright-field microscopy, samples are near-transparent, and it suffices to treat them as

pure phase objects and consider only the contributions of PSF_P [11,13,24]. The phase PSF is phenomenologically modeled in Ref. [11]. It is shown to depend on a constant phase caused by the difference in refractive index between the sample and the medium $\delta = (4\pi w/3\lambda)(n_{\text{sample}} - n_{\text{medium}})$, where w is the thickness of the sample. In Section 2.C.1, it will be shown that in the setup used here, the method does not depend on the refractive index or on the material of the unknown objects. It will be shown experimentally that the shift δ is negligible. This is important for biological applications, since cells will likely have refractive indices different from the calibration objects.

It will also be shown experimentally (in Section 2.C.2) that the method yields correct results when used to measure an object with geometry different from the spherical calibration objects. Theoretically, this can be attributed to the relation between the PSF and the line spread function (the distribution of light created by a line in the image). The line spread function can be calculated from the PSF, but for most imaging systems, these two quantities are indistinguishable [25]. It is common practice to model the PSF of a sphere using a Gaussian [11,26,27], which has a Gaussian line spread function with the same width [25]. Again, this is important for biological applications in which we want to measure cylindrical objects such as neurites.

While this method relies on the collection of the 3D PSF (which is a stack of images), it does not rely on detailed modeling of the PSF. The imaging conditions here are also more general than those in many previous studies of biological systems with diffraction patterns that rely on knowledge of sample position in either the near-field or the far-field regime [28–30].

2. MATERIALS AND METHODS

A. Experimental Setup

1. Optical Images

All optical images were acquired in bright-field with an inverted optical microscope (Olympus 71-X, equipped with a 100× oil-immersion objective, NA = 1.44) and a CCD camera (Cascade II, Photometrics). The camera captures 512 × 512 pixel images with 16 × 16 μm^2 pixel size. At the sampling plane, the spatial sampling width is 16 μm/100 = 160 nm. Samples were illuminated by a 12 V halogen bulb. Experiments were performed with a common microscope setup; no special lenses or detectors were needed.

2. Neuronal Cultures

All procedures were approved by McGill University's Animal Care Committee and conformed to the guidelines of the Canadian Council of Animal Care. Neuron samples containing PDL-coated beads were prepared following procedures outlined in Refs. [7,15,20]. Samples were imaged in cell media.

3. SEM Images

Samples were imaged with a FEI Quanta 450 Environmental Scanning Electron Microscope (FE-ESEM) located at the Facility for Electron Microscopy Research at McGill University. To avoid charging effects, samples were coated with 4 nm platinum with a Leica EM ACE 600 High Vacuum Sputter Coater.

B. Diameter Estimation

A procedure for finding the diameter of an object by comparing its diffraction pattern to those of a set of beads in a series of out-of-focus images is described in this section. Throughout the description, we refer to Fig. 2 for a schematic of the procedure. This method requires a so-called "test image," a single image that contains two objects [see Fig. 2(a)]. One object is of unknown dimension ("unknown object"); its width will be determined with the method, and the other object is a bead of known dimension ("known bead"). The method further requires a "calibration series" of images [again see Fig. 2(a)]. This is an image stack of a set of beads of various known dimensions as a function of defocus. Each image in the stack is acquired at a different objective-focal plane separation z (i.e., different axial positions). One of the beads in this calibration series must be of the same dimension as the known bead in the test image. Using this calibration series and the known bead, one can match the axial position of the microscope when the unknown object is imaged to an axial position in the calibration series, as described in Ref. [31]. Since the calibration series contains beads of different and known diameters, this allows the determination of the unknown bead diameter. Surprisingly, as will be shown below, the method is effective down to ∼ 100 nm with an accuracy ∼ 15%, with potential of improvement if a more sophisticated camera and single wavelength illumination are used. In the following, the process is described step by step [again see Fig. 2].

First the 2D images of all the beads in the test image and the calibration series are converted to 1D arrays called radius vectors [31]. Each 2D image of a bead, which is an intensity function of the position on the image in pixels, has an associated radius vector. Each element of a radius vector I is the average intensity about an annulus concentric with the bead, and the position of the element in the vector is the radius of the annulus as measured from the bead center. See Fig. 2(b) for an example of a 2D image and its associated radius vector. To convert a bead image to a radius vector, we first isolate the individual bead from the initial field of view to a smaller region and identify its center (in pixels) with a custom-made centroid tracking algorithm, as described in Refs. [31–33]. We then assign cartesian coordinates to the circular bead image (with the origin at the bead center) and convert that to a rectangle in the space defined by polar coordinates. The rectangle is collapsed to a vector by averaging along lines of constant θ—this is the radius vector, and it contains the same information as the 2D image. To minimize the effects of variations in background intensity, the radius vectors were normalized by dividing each element in the vector by the element with maximum intensity.

For each bead labeled D in the calibration series, a matrix M^D is constructed by taking the radius vector $[I_{1z_k} I_{2z_k} \ldots I_{nz_k}]^T$ of the bead at each axial position z_k and inserting it into columns of a matrix. The collection of M^D matrices is shown in curly brackets {} in Fig. 2, and an example of a radius vector is highlighted in a dashed red square. The results presented in this work are obtained with a calibration series of images at 16 different axial positions of four differently sized beads, so we have

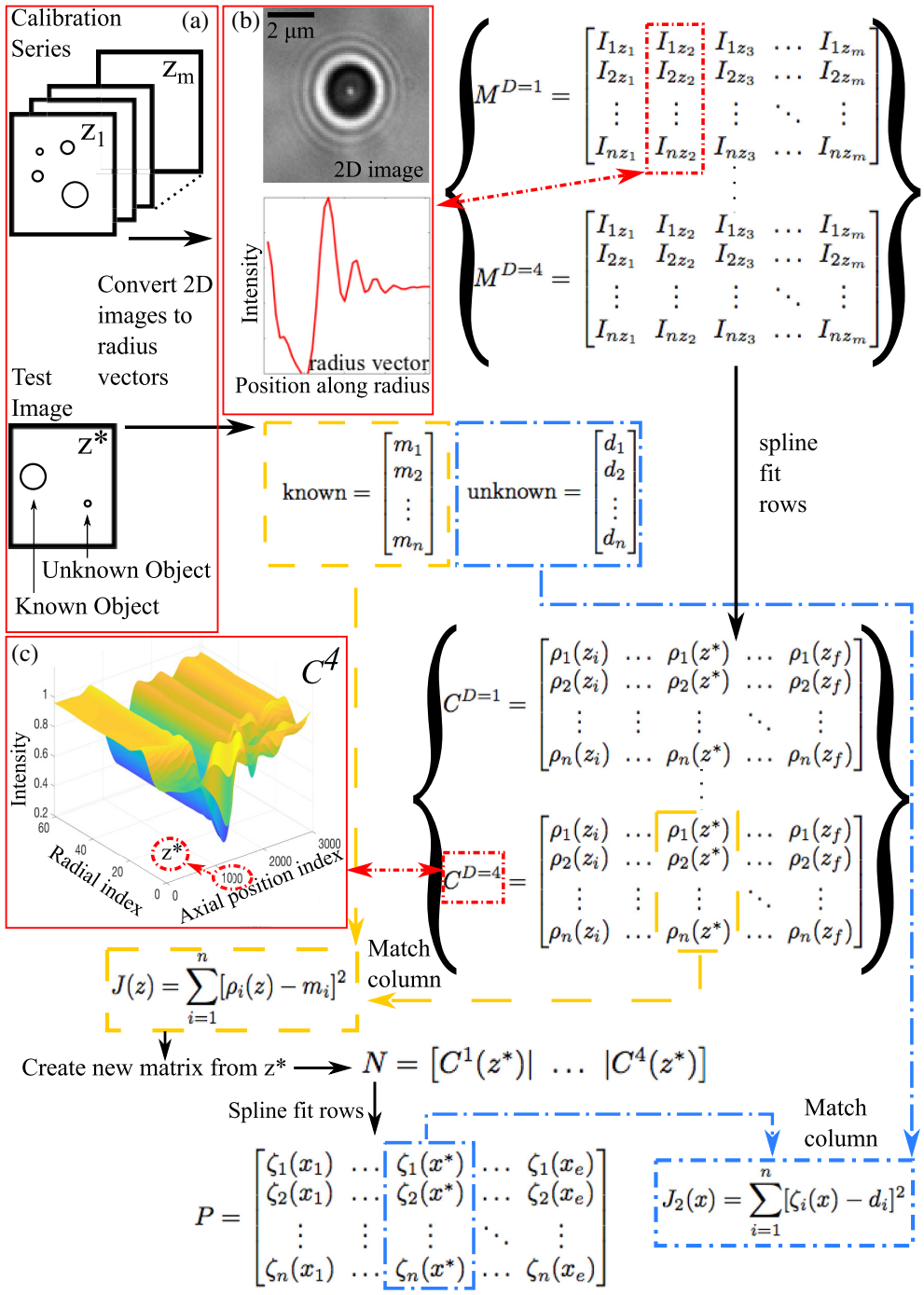

Fig. 2. Schematic of procedure to extract bead diameter from out-of-focus images. (a) Sketch of a test image containing beads of known and unknown dimensions and a calibration series, which is an axial stack of images, labeled by z, of beads of known dimensions. (b) Image of a bead and its corresponding radius vector. Curly brackets: for each bead in the calibration series, a matrix M^D is constructed by concatenating the radius vectors from each image z_k of the calibration series. The rows of the M^D matrices are spline fit to create C^D (also shown in curly brackets). An example of a C^D matrix is plotted in (c). The axial position of the test image z^* is found by matching the radius vector of the known bead to the column of the appropriate matrix C^D by minimizing $J(z)$ (gold boxes). Using z^*, N is constructed and spline fit to obtain P. The radius vector of the unknown object is compared to each column of P via $J_2(x)$ (blue boxes). The value of x that minimizes J_2 is the diameter of the unknown object.

$4 \times M^D$ matrices each with 16 columns indexed by z_k, where $k = 1, \ldots, 16$. The rows of each of these matrices are spline fit using cubic interpolation to create a new series of matrices C^D, also shown in curly brackets {} in Fig. 2. An example of a C^D matrix is displayed as a mesh plot in Fig. 2(c). Note that the success of this method does not rely on acquisition of the different calibration images at a fixed interval in z; one does not need a precision motorized focus control for this method to work.

The axial position z^* of the test image is found relative to the calibration series following the method described in Ref. [31]. The range of possible axial positions for the test image is ~ 10 μm above or below the point where the known object is in focus. The radius vector $[m_1 m_2 \dots m_n]^T$ of the known bead in the test image is compared to each of the columns of the $C^{D=4}$ matrix that corresponds to the size of the unknown bead ($D = 4$, where 4 labels the bead in the calibration series that matches the bead of known dimension in the test image). This comparison is made via

$$J(z) = \sum_{i=1}^{n} [\rho_i(z) - m_i]^2, \tag{3}$$

where we have adopted the notation in Ref. [31], and $[\rho_1(z)\rho_2(z) \dots \rho_n(z)]^T$ are the columns of C^4. Gold, dashed arrows and boxes represent this matching procedure in Fig. 2. The known vector and the relevant column in C^4 are in gold, dashed boxes and are connected to J, also in a gold box, by gold arrows. The axial position z^* is found by minimizing $J(z)$.

Next a new matrix, N, is constructed by extracting and concatenating the columns with index z^* from each of the C^D matrices. The columns of this new matrix are thus each associated with a different bead diameter. For the results presented here, we had four differently sized beads (diameters of 0.2 to 10 μm) in the calibration series generating four C^D matrices. Each matrix contributes a column to N, so here N will have four columns. The rows of N are again spline fit using cubic interpolation to construct a diameter-calibration matrix P with columns $[\zeta_1(x)\zeta_2(x) \dots \zeta_n(x)]^T$ indexed by diameter x. Note that we use a built-in extrapolation algorithm in MATLAB to evaluate radii outside the range of the calibration beads.

As before, the radius vector of the unknown bead in the test image, $[d_1 d_2 \dots d_n]^T$ (in a blue, dashed box in Fig. 2), is matched to a column of the diameter-calibration matrix P (also in a blue, dashed box) by minimizing

$$J_2(x) = \sum_{i=1}^{n} [\zeta_i(x) - d_i]^2. \tag{4}$$

The value of x that minimizes $J_2(x)$ is the diameter of the unknown bead. The matched quantities are shown in blue in Fig. 2.

C. Validation of Method

The method is validated by applying it to find the diameters of objects of different dimensions and comparing the results to correlative SEM measurements; the results are shown in Fig. 3. Each histogram in Fig. 3 is from applying the method to beads of different nominal sizes from the manufacturer. An "unknown" bead was imaged multiple times at multiple different z values, and its diameter was determined using the method detailed above. The histogram in Fig. 3 is the combination of such measurements of several beads (4-5) of the same nominal diameter (e.g., the histogram for nominal diameter of 200 nm is from five different beads, each imaged at ~ 20 different z values).

Figure 3 shows the capability of this method to measure diameters down to 100 nm, the smallest size of object tested.

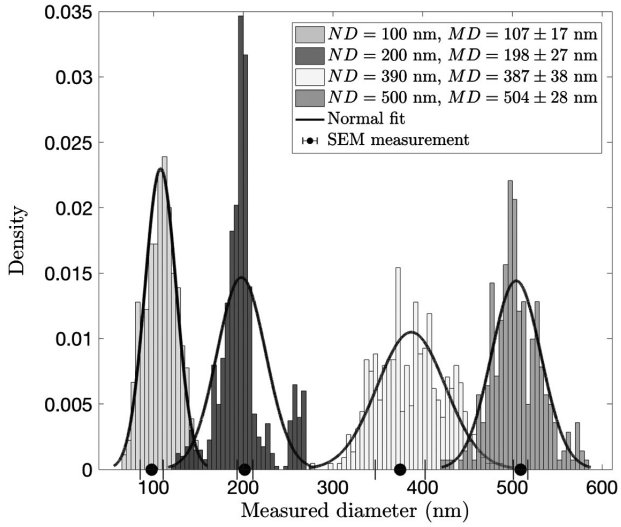

Fig. 3. Histograms of bead diameters as measured by the diffraction method. Each histogram corresponds to measurements of a set of beads (4-5) with the same nominal diameter (labeled "ND" in legend). The means and standard deviations of each histogram are also given in the legend, labeled "MD = mean ± SD", where "MD" is for "measured diameter." Several beads of each size are also measured by SEM; the means and standard deviations of these measurements are shown for comparison (black dots). We also plot normal distributions (black lines) of width and average identical to measured diameters.

The spread of each distribution is due to the combination of noise from the camera pixels and from sampling below the Nyquist limit. In Ref. [31], it is shown that the variance of pixel noise in the axial position estimation decays exponentially with the number of pixels in the radius vector, and so will the variance of pixel noise in the diameter estimation. Furthermore, this quantity is dependant on the objective-sample plane separation or z. It increases with increasing z and is at a minimum when the bead is in focus. Since larger beads can be imaged across a greater range of z values, their histograms include data from greater values of z, which increases their spread. However, we note that the relative standard deviation of each histogram ultimately decreases with increasing bead size. Noise from sampling in this case should not depend on bead radius and will be discussed in a later section.

In Figs. 4 and 5, the diffraction method is validated by comparing the results to SEM measurements. In Fig. 4, we image the exact same sets of beads with the optical microscope and the SEM. This is done for beads with nominal diameters of 100 and 200 nm. The method is found to be accurate; in the case of the 100 nm bead, the percent difference between the two methods ranged from : 2%–21%, and in the 200 nm case, the percent differences were ~ 4%.

1. Verification of Different Materials

In Fig. 5(a), the effects of the object material and the medium on the measured diameters are investigated. We apply the diffraction method to unknown beads of different materials—polystyrene, silica glass, and silver—and find that the measured diameters match those obtained by SEM to within error. The

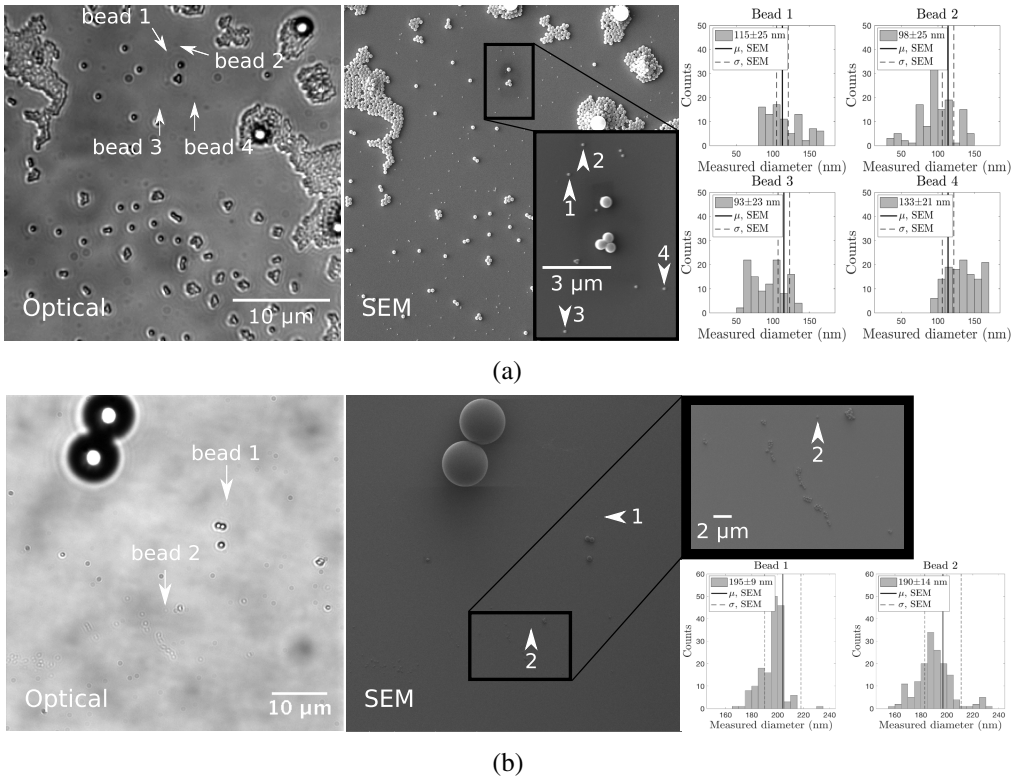

Fig. 4. Validation of the method with SEM measurements. The same beads are imaged with an optical microscope and a SEM. Histograms are diameters of beads 1, 2, 3, 4 (white arrows) in (a) and beads 1, 2 (white arrows) in (b) measured with the diffraction method. The counts in the histograms are from taking measurements from images at different objective-sample plane separations. The means and standard deviations of the histograms are in the legends. The SEM results are plotted with the histograms for comparison; the solid lines represent the measured values, and dashed lines are the uncertainties from the pixel size. (a) We confirm the capability of the method to measure beads with nominal diameters of 100 nm. The percent differences in the diameters as measured by the diffraction method and SEM range from ∼ 2% (bead 1) to ∼ 21% (bead 3). (b) We apply the method to beads with a nominal diameter of 200 nm and report percent differences of ∼ 4% between the two measurement methods.

diffraction method is also applied to polystyrene beads in water, and the diameters found are consistent with SEM results. This demonstrates that the method is robust in terms of the refractive index of the material to be measured and the environment in which it is imaged.

2. *Verification of Different Geometries*

It was also checked that the diffraction method can be applied to an unknown object with a geometry different from the calibration beads, since neurites are cylindrical rather than spherical. The diffraction method is applied to a borosilicate fiber, and a diameter of 636 ± 64 nm is found, which is consistent with the diameter of 656 nm measured by SEM imaging [see Fig. 5(b)].

D. Estimation Error

In the application of the method to cellular material, we take the standard deviation of repeated measurements to be the error in diameter; this is at the ∼ 15% level for ∼ 200 nm objects. This error is due to a combination of random noise from the camera and error from spatial sampling. Pixel noise enters into the radius vectors of the beads and affects the axial position estimation variance, as described in Ref. [31], as well as the diameter estimation variance. Our measurements are also subject to error due to spatial sampling at frequencies below the Nyquist limit. This occurs in two places. First, in the determination of the axial position, each image in the calibration series provides columns to separate M^D matrices (each image provides one column for each different bead size). We assume that we are sampling discrete z values of some continuous function of z. In our setup, the step size between images is controlled by manually turning the focus knob, and so we are unable to sample steps below the Nyquist critical sampling distance in the axial direction. Precise control of the step size, e.g., with a piezo stage, could lead to improved measurement error. Second, the construction of the N matrix introduces sampling noise. Here the step size between different columns of N is determined by the sizes of the calibration beads. To eliminate this noise, we would require many more different bead sizes.

We experimentally investigate the effects of pixel noise, inaccurate bead centers, and bead position in the field of view. We find that the variance caused by each of these factors is less than or equal to the variance observed in measurements (data not shown). We considered the effect of spatial sampling by measuring the diameter with (separately) modified M^D and N matrices. We excluded up to half the columns of M^D and found that the variance in the diameter was stable. This could indicate we are near the maximum amount of noise from spatial

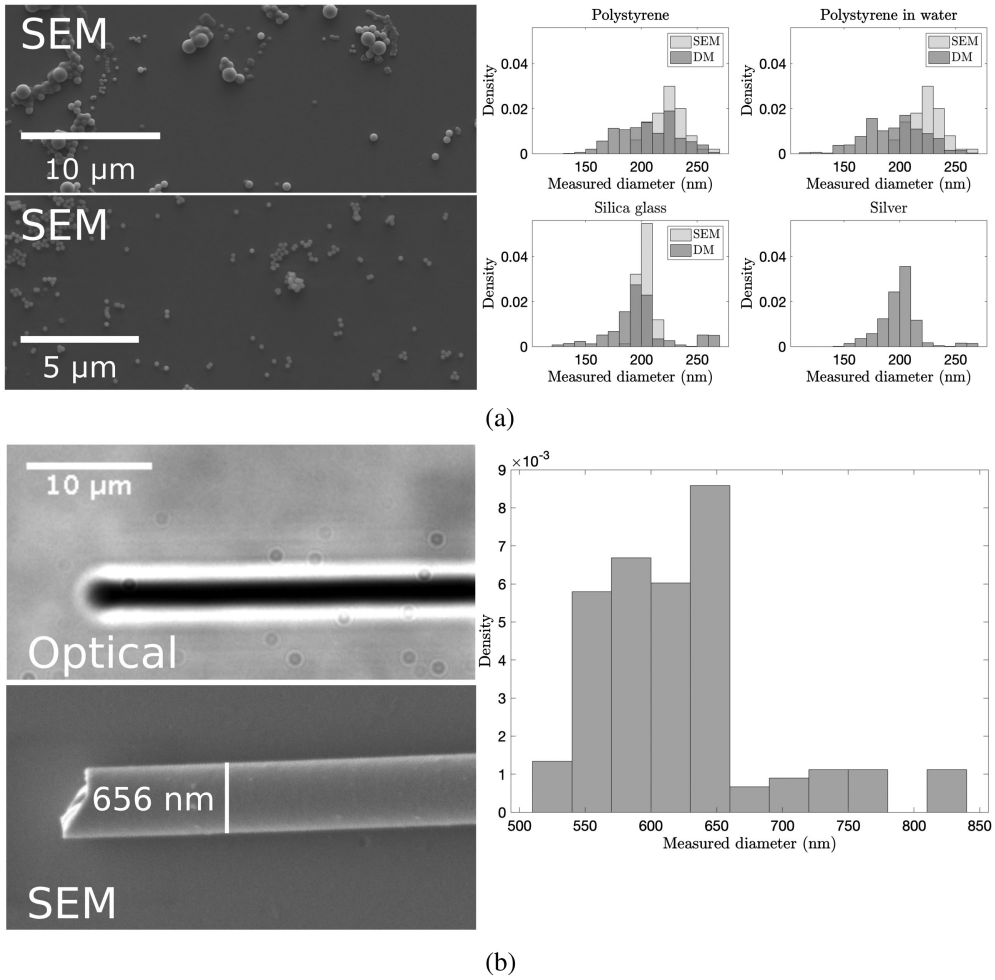

Fig. 5. Verification of the method with SEM measurements. (a) Left: SEM images of (top) polysytrene beads and (bottom) silica glass beads. Histograms of diameters of beads of different materials measured by SEM and by diffraction method (DM). DM data are from images at different objective-focal plane separations of five different beads for each material. The two methods agree to within one standard deviation. (b) Optical and SEM images of a borosilicate fiber and the corresponding DM measurements. This confirms that the DM can be applied to unknown objects that have geometries different from the calibration objects.

sampling in the axial direction. Ultimately, improving sampling width in both M^D and N dimensions could improve the measurement error.

3. APPLICATION TO DETERMINING THE DIAMETER OF NEURITES

This method is applied to extract diameters of artificially generated neurites. These long cylindrical structures are created by a procedure described in Refs. [7,15,16], with the essential details summarized here. In brief, a PDL-coated polystyrene bead (10 μm in our measurements) is put in contact with an axon or a dendrite for sufficient time to form a synapse at the bead–cell interface. When the cellular structure is moved relative to the bead, an auxiliary structure, the neurite, is induced. In passing, we note that these pulled neurites cannot be distinguished structurally or functionally from naturally grown neurites [7,15]. Hippocampal axons are typically ~ 1 μm in diameter, and the diameters of the pulled neurites branching from these can fall below the diffraction limit of our optical microscope. One major motivation for developing this method was to answer the question, "Can we control the diameter of the pulled neurites by changing the pulling rate?" This could in turn clarify the dependence of action potential propagation on neurite diameter [34,35].

To determine the diameters, neurites and their corresponding diffraction fringes are identified by eye and isolated from an image (see Fig. 1). These image segments are then rotated so that the axis of the neurite is aligned with the horizontal axis. We then measure intensity versus pixel along lines perpendicular to the axis of the neurite (such that each pixel along the horizontal axis of the neurite has a corresponding line profile). Figure 1(d) is the average of all the line profiles from Fig. 1(c). From each line profile, two line profiles are created by splitting the original line profile at the center of the neurite. The neurite center is estimated by finding the midpoint between the first two extrema in the intensity profile [see Fig. 1(d)]. Thus, for each pixel along the neurite axis, there are two line profiles of intensity versus pixel. These line profiles are taken to be the radius vectors of the unknown object, $[d_1 d_2 \ldots d_n]^T$ in Section 2.B. From each line

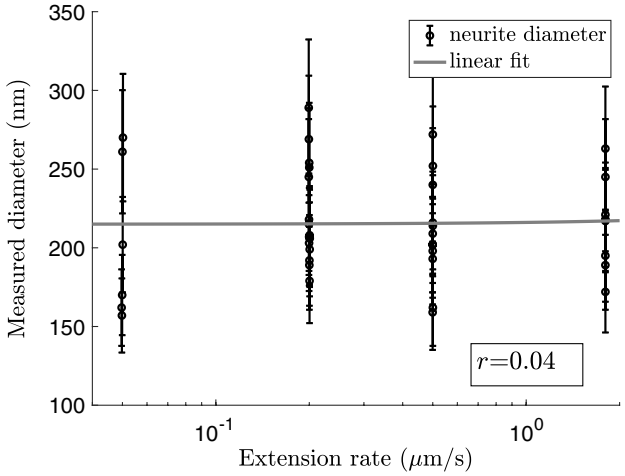

Fig. 6. Diameters of neurites measured with the diffraction method for different extension rates (0.05 μm/s, 0.2 μm/s, 0.5 μm/s, 1.8 μm/s) plotted on a log scale. The distribution of the neurites is the same for each extension rate, as determined by the Kruskal–Wallis test. The Pearson correlation coefficient between the logarithm of extension rate and neurite diameter is $r = 0.04$, which indicates that the diameter does not change monotonically with extension rate. The linear relation associated with the correlation coefficient is plotted in gray.

profile, we extract a diameter measurement. The average of the diameters found from the set of line profiles above the neurite center is compared to the average of the diameters found from the set below the neurite center to verify they match within error. The measured diameters are shown in Fig. 6.

To determine if the neurite has a constant diameter along the entire box size, diameters for the mean of each line profile and its n-neighbors for $n = 1, \ldots, L_x$, where L_x is the horizontal dimension of the box in pixels, are computed. For each moving average size n, the variance of the corresponding diameters is computed. As long as this relation decreases monotonically, the neurite diameter is constant within the box.

This method of measuring the neurite radius lends naturally to our pulling procedure. A bead resting on an axon is pulled, and the initial axial position of the bead is held constant so the neurite is at the base of the bead. Thus, the bead and the neurite have the same relative positions as the known and unknown objects in the test image. Here we consider only neurites that are of constant diameter within the box. This is because this method cannot distinguish between diameter differences due to an intrinsic size change along the neurite or due to different segments of the neurite lying in different focal planes, unless there is another bead present in the image besides the one on the microneedle tip that can be used as a second reference.

Figure 6 shows the diameters of neurites created by extending the neurite at different rates. Surprisingly, we see the spread in the measured diameters is the same over a 10-fold increase in extension rate. This is confirmed with the Kruskal–Wallis test ($p = 0.69$), which determines that the diameters, grouped by extension rate, are all drawn from the same distribution. The Pearson correlation coefficient between the logarithm of the extension rate and neurite diameter is $r = 0.04$, which confirms that the diameter does not change monotonically with extension rate. Therefore, extension rate in the range tested is not an important predictor of a cross-sectional area of mechanically created neurites.

4. CONCLUSION

In this work, a method to obtain the size of objects that are smaller than the optical diffraction limit is presented. This tool relies on matching the diffraction patterns of test objects to those in a series of out-of-focus optical images. In particular, this method does not require fluorescent labeling probes. This procedure enables us to measure objects with 100 nm diameters, which is similar to the size of structures that can be measured with classic structured illumination microscopy (SIM) [9,36]. While in theory it is possible to obtain a 3D profile of objects with this method, this was not demonstrated here. We note however the limitations of this method with respect to the family of super-resolution techniques (see Ref. [9] for a review). The method is unable to resolve different objects clustered together at the 100 nm length scale; it can merely extract their collective size. This method is thus best applied to structures that are isolated in the field of view, a condition met in, e.g., optical tweezers experiments. This is a requirement similar to the method presented in Ref. [37], a super-resolution coherent diffractive imaging technique. In the same vein, our method cannot discern individual components within a cell. Reference [38] demonstrated a method to image objects through scattering media, also with a reference object, and could potentially be combined with this method to image cellular structures. Fluorescence microscopy could also be used in conjunction with this technique to provide finer details of the cellular architecture and capture rapid motions in cells [39]. While fluorescence microscopy use is widespread, note that neurons are photo-sensitive [40], and fluorescence microscopy relies on exogenous labels, making it sensitive to effects of phototoxicity and photostability from the excitation light [11,41].

The photosensitivity of neurons is also a consideration in the application of this technique with dark-field microscopy, which requires high intensity illumination [42]. While in theory this method could be used with dark-field, a series of checks such as those presented here would need to be performed to determine how to account for the differences in the properties of the samples and the calibration objects (index of refraction and geometry).

This method is not an alternative to super-resolution microscopy, which is extremely powerful in its capabilities. Reference [43], for example, achieved super-resolution and enhanced the ratio of field of view to pixel size required to achieve Nyquist sampling at the resolution of the image with a pixel super-resolution algorithm that uses out-of-focus images, in the context of coherent microscopy. Our method may, however, be more convenient in certain contexts. Bright-field microscopy is simple and allows the continuous observation of unstained samples for long periods of time [11]. Many super-resolution techniques require specialized equipment such as lasers, and both single molecule localization microscopy (SMLM) and stimulated emission depletion microscopy (STED) require specialized probes that can be sample-dependent [9,36]. Finding a

good sample-preparation recipe to perform the desired experiment can be a multi-month enterprise and can ultimately limit which experiments can be performed [44,45].

Other works have used bright-field microscopy to achieve sub-resolution measurements. Amazingly, Ref. [46] demonstrated the visualization of microtubules, cylinders of ∼ 25 nm diameter, with a conventional bright-field setup. This was achieved through so-called computer-enhanced bright-field imaging, which involves averaging over multiple frames, background subtraction, spatial filtering, and smoothing and enhancing images with spatial convolution routines. We present a different method that can be applied to structures suspended above the coverslip, but we note that our results could be improved by adopting the techniques outlined in Ref. [46] as well as tools from machine learning. Reference [13] also detailed a method to measure cell surface fluctuations by defocusing a bright-field microscope, but this technique does not measure sub-resolution structures. Reference [47] demonstrated a method for enhanced optical resolution in the far-field regime using a confocal laser scanning microscopy setup.

This method is applied to characterize the deformability of mechanically created neurites. Within our statistics, we do not find that the geometry of induced neurites depends on the pull speed at which they were created. The independence of neurite width and pull speed is significant for fundamental questions of axonal growth. The fact that speed is not a factor in neurite width implies that there is something else governing the size of neurites. All neurites in these experiments were induced with 10 μm-sized beads. An avenue of future study is to repeat these measurements with different bead sizes to see if this is a factor determining neurite width.

Funding. Natural Sciences and Engineering Research Council of Canada (NSERC CGSD3-490080-2016); Fonds de Recherche du Québec - Nature et Technologies.

Acknowledgment. We thank David Liu and Weawkamol Leelapornpisit at the Facility for Electron Microscopy Research of McGill University for their invaluable help in sample preparation. We also thank Xavier Capaldi for help with SEM measurements.

Disclosures. The authors declare that there are no conflicts of interest related to this paper.

REFERENCES

1. J. Dai and M. P. Sheetz, "Mechanical properties of neuronal growth cone membranes studied by tether formation with laser optical tweezers," Biophys. J. **68**, 988–996 (1995).
2. J. Dai and M. P. Sheetz, "Membrane tether formation from blebbing cells," Biophys. J. **77**, 3363–3370 (1999).
3. B. Pontes, N. B. Viana, L. T. Salgado, M. Farina, V. M. Neto, and H. M. Nussenzveig, "Cell cytoskeleton and tether extraction," Biophys. J. **101**, 43–52 (2011).
4. B. Pontes, Y. Ayala, A. C. C. Fonseca, L. F. Romão, R. F. Amaral, L. T. Salgado, F. R. Lima, M. Farina, N. B. Viana, V. Moura-Neto, and H. M. Nussenzveig, "Membrane elastic properties and cell function," PLoS One **8**, e67708 (2013).
5. B. Pontes, P. Monzo, L. Gole, A.-L. Le Roux, A. J. Kosmalska, Z. Y. Tam, W. Luo, S. Kan, V. Viasnoff, P. Roca-Cusachs, L. Tucker-Kellogg, and N. C. Gauthier, "Membrane tension controls adhesion positioning at the leading edge of cells," J. Cell Biol. **216**, 2959–2977 (2017).
6. D. Cuvelier, I. Derényi, P. Bassereau, and P. Nassoy, "Coalescence of membrane tethers: experiments, theory, and applications," Biophys. J. **88**, 2714–2726 (2005).
7. M. Anthonisen, M. Rigby, M. H. Sangji, X. Y. Chua, and P. Grütter, "Response of mechanically-created neurites to extension," J. Mech. Behavior Biomed. Mater. **98**, 121–130 (2019).
8. R. E. Thompson, D. R. Larson, and W. W. Webb, "Precise nanometer localization analysis for individual fluorescent probes," Biophys. J. **82**, 2775–2783 (2002).
9. C. Leterrier, P. Dubey, and S. Roy, "The nano-architecture of the axonal cytoskeleton," Nat. Rev. Neurosci. **18**, 713 (2017).
10. Y. Zhang, T. Huang, D. M. Jorgens, A. Nickerson, L.-J. Lin, J. Pelz, J. W. Gray, C. S. López, and X. Nan, "Quantitating morphological changes in biological samples during scanning electron microscopy sample preparation with correlative super-resolution microscopy," PLoS One **12**, e0176839 (2017).
11. C. N. H. Candia and B. Gutiérrez-Medina, "Direct imaging of phase objects enables conventional deconvolution in bright field light microscopy," PLoS One **9**, e89106 (2014).
12. U. Agero, L. Mesquita, B. Neves, R. Gazzinelli, and O. Mesquita, "Defocusing microscopy," Microsc. Res. Tech. **65**, 159–165 (2004).
13. U. Agero, C. Monken, C. Ropert, R. Gazzinelli, and O. Mesquita, "Cell surface fluctuations studied with defocusing microscopy," Phys. Rev. E **67**, 051904 (2003).
14. A. L. Lucido, F. S. Sanchez, P. Thostrup, A. V. Kwiatkowski, S. Leal-Ortiz, G. Gopalakrishnan, D. Liazoghli, W. Belkaid, R. B. Lennox, P. Grutter, C. C. Garner, and D. R. Colman, "Rapid assembly of functional presynaptic boutons triggered by adhesive contacts," J. Neurosci. **29**, 12449–12466 (2009).
15. M. H. Magdesian, M. Anthonisen, G. M. Lopez-Ayon, X. Y. Chua, M. Rigby, and P. Grütter, "Rewiring neuronal circuits: a new method for fast neurite extension and functional neuronal connection," J. Visualized Exp. **13**, e55697 (2017).
16. M. Rigby, M. Anthonisen, X. Chua, A. Kaplan, A. Fournier, and P. Grütter, "Building an artificial neural network with neurons," AIP Adv. **9**, 075009 (2019).
17. R. Bernal, P. A. Pullarkat, and F. Melo, "Mechanical properties of axons," Phys. Rev. Lett. **99**, 018301 (2007).
18. Y. Zhang, K. Abiraman, H. Li, D. M. Pierce, A. V. Tzingounis, and G. Lykotrafitis, "Modeling of the axon membrane skeleton structure and implications for its mechanical properties," PLoS Comput. Biol. **13**, e1005407 (2017).
19. S. Javid, A. Rezaei, and G. Karami, "A micromechanical procedure for viscoelastic characterization of the axons and ECM of the brainstem," J. Mech. Behavior Biomed. Mater. **30**, 290–299 (2014).
20. M. H. Magdesian, G. M. Lopez-Ayon, M. Mori, D. Boudreau, A. Goulet-Hanssens, R. Sanz, Y. Miyahara, C. J. Barrett, A. E. Fournier, Y. De Koninck, and P. Grütter, "Rapid mechanically controlled rewiring of neuronal circuits," J. Neurosci. **36**, 979–987 (2016).
21. B. E. Saleh and M. C. Teich, *Fundamentals of Photonics* (Wiley, 2019).
22. M. Born and E. Wolf, *Principles of Optics* (1980), vol. **6**.
23. H. C. Hulst and H. C. van de Hulst, *Light Scattering by Small Particles* (Courier Corporation, 1981).
24. N. Streibl, "Three-dimensional imaging by a microscope," J. Opt. Soc. Am. A: **2**, 121–127 (1985).
25. S. W. Smith, *The scientist and engineer's guide to digital signal processing* (California Technical Pub. 1997).
26. F. Aguet, D. Van De Ville, and M. Unser, "Model-based 2.5-d deconvolution for extended depth of field in brightfield microscopy," IEEE Trans. Image Process. **17**, 1144–1153 (2008).
27. J. Degerman, E. Winterfors, J. Faijerson, and T. Gustavsson, "A computational 3D model for reconstruction of neural stem cells in bright-field time-lapse microscopy," Proc. SPIE **6498**, 64981E (2007).
28. R. Baskin, K. Roos, and Y. Yeh, "Light diffraction study of single skeletal muscle fibres," Biophys. J. **28**, 45–64 (1979).
29. C. Sundell, Y. Goldman, and L. Peachey, "Fine structure in near-field and far-field laser diffraction patterns from skeletal muscle fibers," Biophys. J. **49**, 521–530 (1986).

30. M. Mihailescu and J. Costescu, "Diffraction pattern study for cell type identification," Opt. Express **20**, 1465–1474 (2012).
31. Z. Zhang and C.-H. Menq, "Three-dimensional particle tracking with subnanometer resolution using off-focus images," Appl. Opt. **47**, 2361–2370 (2008).
32. M. K. Cheezum, W. F. Walker, and W. H. Guilford, "Quantitative comparison of algorithms for tracking single fluorescent particles," Biophys. J. **81**, 2378–2388 (2001).
33. A. von Diezmann, Y. Shechtman, and W. Moerner, "Three-dimensional localization of single molecules for super-resolution imaging and single-particle tracking," Chem. Rev. **117**, 7244–7275 (2017).
34. P. D. Maia and J. N. Kutz, "Compromised axonal functionality after neurodegeneration, concussion and/or traumatic brain injury," J. Comput. Neurosci. **37**, 317–332 (2014).
35. J. Tian, G. Huang, M. Lin, J. Qiu, B. Sha, T. J. Lu, and F. Xu, "A mechanoelectrical coupling model of neurons under stretching," J. Mech. Behavior Biomed. Mater. **93**, 213–221 (2019).
36. L. Schermelleh, R. Heintzmann, and H. Leonhardt, "A guide to super-resolution fluorescence microscopy," J. Cell Biol. **190**, 165–175 (2010).
37. A. Szameit, Y. Shechtman, E. Osherovich, E. Bullkich, P. Sidorenko, H. Dana, S. Steiner, E. B. Kley, S. Gazit, T. Cohen-Hyams, S. Shoham, M. Zibulevsky, I. Yavneh, Y. C. Eldar, O. Cohen, and M. Segev, "Sparsity-based single-shot subwavelength coherent diffractive imaging," Nat. Mater. **11**, 455–459 (2012).
38. X. Xu, X. Xie, H. He, H. Zhuang, J. Zhou, A. Thendiyammal, and A. P. Mosk, "Imaging objects through scattering layers and around corners by retrieval of the scattered point spread function," Opt. Express **25**, 32829–32840 (2017).
39. Y. Park, G. Popescu, K. Badizadegan, R. R. Dasari, and M. S. Feld, "Diffraction phase and fluorescence microscopy," Opt. Express **14**, 8263–8268 (2006).
40. E. S. Boyden, F. Zhang, E. Bamberg, G. Nagel, and K. Deisseroth, "Millisecond-timescale, genetically targeted optical control of neural activity," Nat. Neurosci. **8**, 1263 (2005).
41. R. Hoebe, C. Van Oven, T. Gadella, Jr., P. Dhonukshe, C. Van Noorden, and E. Manders, "Controlled light-exposure microscopy reduces photobleaching and phototoxicity in fluorescence live-cell imaging," Nat. Biotechnol. **25**, 249 (2007).
42. T. J. F. William Chambers and M. W. Davidson, *Nikon – Stereomicroscopy – Darkfield Illumination* (2019).
43. H. Wang, Z. Göröcs, W. Luo, Y. Zhang, Y. Rivenson, L. A. Bentolila, and A. Ozcan, "Computational out-of-focus imaging increases the space–bandwidth product in lens-based coherent microscopy," Optica **3**, 1422–1429 (2016).
44. G. Lukinavičius, L. Reymond, E. D'este, A. Masharina, F. Göttfert, H. Ta, A. Güther, M. Fournier, S. Rizzo, H. Waldmann, C. Blaukopf, C. Sommer, D. W. Gerlich, H.-D. Arndt, S. W. Hell, and K. Johnsson, "Fluorogenic probes for live-cell imaging of the cytoskeleton," Nat. Methods **11**, 731 (2014).
45. A. Chazeau, E. A. Katrukha, C. C. Hoogenraad, and L. C. Kapitein, "Studying neuronal microtubule organization and microtubule-associated proteins using single molecule localization microscopy," in *Methods in Cell Biology* (Elsevier, 2016), vol. **131**, pp. 127–149.
46. B. Gutiérrez-Medina and S. M. Block, "Visualizing individual microtubules by bright field microscopy," Am. J. Phys **78**, 1152–1159 (2010).
47. X. Xie, Y. Chen, K. Yang, and J. Zhou, "Harnessing the point-spread function for high-resolution far-field optical microscopy," Phys. Rev. Lett. **113**, 263901 (2014).